Frequency-Constrained Energy Management System for Isolated Microgrids

Samuel Córdova, *Student Member, IEEE,* Claudio A. Cañizares, *Fellow, IEEE,* Álvaro Lorca, *Member, IEEE,* and Daniel E. Olivares, *Member, IEEE*

***Abstract*—Second-to-second power imbalances stemming from renewable generation can have a large impact on the frequency regulation performance of isolated microgrids, as these are characterized by low inertia and, more commonly nowadays, significant renewable energy penetration. Thus, the present paper develops a novel frequency-constrained Energy Management System (EMS) that takes into account the impact of short-term power fluctuations on the microgrid's operation and frequency regulation performance. The proposed EMS model is based on accurate linear equations describing frequency deviation, rate-of-change-of-frequency, and regulation provision in daily microgrid operations. Dynamic simulations on a realistic CIGRE benchmark test system show the economic and reliability benefits of the presented EMS model, highlighting the need of incorporating fast power fluctuations and their impact on frequency dynamics in EMSs for sustainable isolated microgrids.**

***Index Terms*—Energy management system, short-term fluctuations, frequency regulation, frequency dynamics, microgrid operation.**

NOMENCLATURE

Superscripts

B	Battery
D	Demand
G	Generator
MG	Microgrid
S, W	Solar and wind generation
χ	Forecast error
$\boldsymbol{r}, \boldsymbol{\partial r}$	Regulation and regulation-ramp
$\uparrow, \downarrow$	Upward and downward

Subscripts and Sets

$b \in \mathcal{B}$	Battery
$g \in \mathcal{G}$	Thermal generator
$h \in \mathcal{H}$	Long dispatch time interval, $\mathcal{H} = \{1, \ldots, H\}$
$h \in \mathcal{H}^{\boldsymbol{r}}$	Subset of the long dispatch time intervals with a finer time resolution (first time steps)
$j \in \mathcal{J}$	Short time interval, $\mathcal{J} = \{1, \ldots, J\}$
$l \in \mathcal{L}$	Partition for piecewise linear battery degradation model

Parameters

C_g^G	Variable generation costs of generator g
C^{LS}	Load shedding costs
C_g^{NL}	No-load costs of generator g
C_g^{SU}, C_g^{SD}	Start-up and shut-down costs of generator g
$\hat{D}_h$	Forecast average demand during dispatch time interval h
E_b	Energy capacity limit of battery b
f_0	Microgrid's nominal frequency
$\overline{\Delta f}$	Absolute frequency deviation limit
IN_g^G	Synchronous inertia of generator g
K^{PF}, K^{PV}	Frequency and voltage sensitivity of loads
K^{VFC}	Proportional gain of voltage frequency controller
M_g^{UP}, M_g^{DN}	Minimum-up and minimum-down times of generator i
$\overline{P}_g^G, \underline{P}_g^G$	Steady-state maximum and minimum power capacity of generator g
$\overline{PT}_g^G, \underline{PT}_g^G$	Transient maximum and minimum power capacity of generator g
$\overline{P}_b^B$	Maximum power capacity of battery b
$\overline{P}_h^W, \overline{P}_h^S$	Maximum available wind and solar average powers during dispatch time interval h
R_g	Ramp limit of generator g
RC_b	Battery replacement cost of battery b
$\overline{RoCoF}$	Absolute Rate of Change of Frequency limit
$S_{b,l}^0$	Initial battery state-of-charge
$\overline{S}_{b,l}$	State-of-charge depth range of battery's b partition l
T^{FC}	Inherent time delay of automatic frequency controllers
ΔT_h	Time step of dispatch time interval h
$\Delta\tau$	Time step of short time intervals $j \in \mathcal{J}$
$\epsilon_\chi, \epsilon_{\boldsymbol{r}}, \epsilon_{\boldsymbol{\partial r}}$	Scaling parameters for forecast error, regulation, and regulation-ramp reserves
η_b^C, η_b^D	Charging and discharging efficiency of battery b
κ_g^G, κ_b^B	Frequency-droop of generator g and battery b
$\tilde{\sigma}_h^\chi, \tilde{\sigma}_h^{\boldsymbol{r}}, \tilde{\sigma}_h^{\boldsymbol{\partial r}}$	Standard deviation of forecast errors, short-term fluctuations, and short-term fluctuation-ramps during dispatch time interval h.

This work was supported by ANID/FONDECYT/1181517, SERC-Chile (ANID/FONDAP/15110019), the Complex Engineering Systems Institute (ANID/FB0816), ANID/PIA/ACT-192094, and NSERC Canada.

S. Córdova and C. A. Cañizares are with the Department of Electrical and Computer Engineering, University of Waterloo, Waterloo, ON N2L 3G1, Canada (e-mail: scordova@uwaterloo.ca; ccanizares@uwaterloo.ca).

A. Lorca is with the Department of Electrical Engineering, the Department of Industrial and Systems Engineering, and the UC Energy Research Center at Pontificia Universidad Católica de Chile, Santiago, Chile (e-mail: alvarolorca@uc.cl).

D. Olivares is with the Faculty of Engineering and Sciences, Universidad Adolfo Ibañez, and the Complex Engineering Systems Institute, Santiago, Chile (e-mail: daniel.olivares@uai.cl).

$\hat{\phi}_{b,l}$	Piecewise linear battery degradation coefficient
$\varphi_h^{\chi}, \varphi_h^{\boldsymbol{r}}$	Expected reserve utilization of forecast error and regulation reserves

Variables

$c_{b,l,h}, d_{b,l,h}$	Battery charging and discharging
$\Delta e_{g,h}$	Change in the expected average power of generator g due to reserve provision
ls_h	Load shedding set-point for dispatch time interval h
$\hat{p}_{g,h}^{G}$	Average power set-point for generator g during dispatch time interval h
$\hat{p}_h^{W}, \hat{p}_h^{S}$	Forecast average wind and solar power during dispatch time interval h
$\Delta p_{g,h}^{G,\chi,\uparrow/\downarrow}$	Upward/downward forecast error reserve provided by generator g
$\Delta p_{g,h}^{G,\boldsymbol{r},\uparrow/\downarrow}$	Upward/downward regulation reserve provided by generator g
$\Delta p_{b,l,h}^{B,C,\chi,\downarrow}$	Downward forecast error reserve provided by increasing battery's charging
$\Delta p_{b,l,h}^{B,C,\boldsymbol{r},\downarrow}$	Downward regulation reserve provided by increasing battery's charging
$\Delta p_{b,l,h}^{B,D,\chi,\uparrow}$	Upward forecast error reserve provided by increasing battery's discharging
$\Delta p_{b,l,h}^{B,D,\boldsymbol{r},\uparrow}$	Upward regulation reserve provided by increasing battery's discharging
$\Delta p_{b,l,h}^{B,C,\chi,\uparrow}$	Upward forecast error reserve provided by decreasing battery's charging
$\Delta p_{b,l,h}^{B,C,\boldsymbol{r},\uparrow}$	Upward regulation reserve provided by decreasing battery's charging
$\Delta p_{b,l,h}^{B,D,\chi,\downarrow}$	Downward forecast error reserve provided by decreasing battery's discharging
$\Delta p_{b,l,h}^{B,D,\boldsymbol{r},\downarrow}$	Downward regulation reserve provided by decreasing battery's discharging
$\Delta p_h^{PF,\boldsymbol{r},\uparrow/\downarrow}$	Upward/downward regulation reserve stemming from load frequency sensitivity
$\Delta p_h^{VFC,\boldsymbol{r},\uparrow/\downarrow}$	Upward/downward regulation reserve stemming from voltage frequency control
$\boldsymbol{r}_h$	Short-term fluctuations during dispatch time interval h
$\boldsymbol{\partial r}_h$	Short-term fluctuation-ramps during dispatch time interval h
$s_{b,l,h}$	Battery state-of-charge
$\Delta s_{b,l,h}$	Change in the expected State-of-Charge of battery's b partition l due to reserve provision
$u_{g,h}$	ON/OFF status of generator g (binary)
$v_{g,h}, w_{g,h}$	Start-up and shut-down of generator g (binary)
$\zeta_h^{\chi}, \zeta_h^{\boldsymbol{r}}, \zeta_h^{\boldsymbol{\partial r}}$	Forecast error, regulation, regulation-ramp reserve requirements
ξ	Uncertainty
$\Phi_{b,l,h}$	Expected resulting battery degradation
$\Delta\phi_{b,l,h}$	Increase in expected battery degradation due to reserve provision
χ_h	Average power forecast error during dispatch time interval h

Acronyms

CoI	Center-of-Inertia
DER	Distributed Energy Resources
EMS	Energy Management System
ERU	Expected Reserve Utilization
FoR	Frequency-or-RoCoF
KLFN	Kasabonika Lake First Nation
MAE	Mean Absolute Error
MILP	Mixed Integer Linear Programming
MPC	Model Predictive Control
QSS	Quasi-Steady-State
RoCoF	Rate-of-Change-of-Frequency
SoC	State-of-Charge
UC	Unit Commitment
UFLS	Under-Frequency Load Shedding
VFC	Voltage Frequency Controller

I. Introduction

MICROGRIDS have attracted considerable attention from researchers and industry given their potential to enable a reliable and efficient integration of Distributed Energy Resources (DER). In this context, several research efforts are currently in progress to enable the secure and economic operation of sustainable isolated microgrids, which have resulted in advanced Energy Management System (EMS) models that account for relevant aspects such as phase imbalance [1], network representations [2], and thermal energy resources [3], amongst others (see [4] and [5] for a thorough literature review).

In contrast to conventional power systems, sustainable isolated microgrids are particularly vulnerable to degraded frequency regulation performance, as these typically exhibit a low inertia and significant renewable integration [6]. This requires the consideration of short-term imbalances in microgrid EMS models, as significant variations in renewable generation can be observed in the second-to-second time frame for geographically close renewable plants [7], which in-turn can cause significant frequency deviations due to the system's low inertia [8]. Consequently, recent microgrid EMS models have proposed going beyond the traditional 5min-1h time scale commonly found in operational models (e.g., [1]–[3]), and also incorporate short-term fluctuations in the time scale of seconds, such that an adequate regulation performance can be provided even in the conditions of low inertia and significant renewable integration (e.g., [9]–[12]).

In [9] and [10], two-stage open-loop EMS models are proposed to manage short-term power fluctuations, for which two decision-making stages are considered; namely, an upper-stage with low time resolution for determining optimal dispatch set-points, and a lower-stage with a more detailed time resolution, in which the dispatch set-points are used as inputs and short-term power fluctuations are managed. Under this approach, both stages are solved independently, i.e., in open-loop, and

thus have the downside of not ensuring feasibility in the lower-stage in the presence of large and fast power fluctuations.

To address the above drawback, [11] proposes a two-stage closed-loop EMS model, for which feasible dispatch set-points are determined by iteratively solving upper and lower stage problems through a constraint generation method, which adds constraints to the upper stage problem if infeasibilities are detected in the lower stage problem. Therefore, by following a closed-loop structure, this approach guarantees that the obtained solutions remain feasible even in the presence of large and fast power fluctuations. However, this results in high computational costs, as the number of variables of the lower stage problem directly depends on the time resolution used for modeling short-term power fluctuations. Thus, practical applications for this type of EMS model can be found only for minute-to-minute power fluctuations, since a more detailed time resolution (e.g., seconds, in the order of fast renewable generation variations) would yield a computationally intractable model with too many decision variables.

To maintain computational tractability while ensuring feasibility for large and fast power fluctuations, [12] presents a computationally efficient EMS model based on alternative low-order representations of short-term fluctuations, for which it is shown that large second-to-second power fluctuations can be accurately managed while maintaining computational tractability for practical applications. However, frequency dynamics are not incorporated in the EMS model, and transient simulations are not considered in the computational experiments. This is particularly relevant for practical applications, as frequency transients can rapidly and significantly deviate from steady-state values in low inertia systems with highly variable renewable energy sources (e.g., see [8]), leaving a pending research gap in this regard.

The explicit modeling of frequency dynamics within operational models is a relatively new research area, with most research being focused on low-inertia bulk-power systems. This has resulted in the development of frequency-constrained Unit Commitment (UC) models that incorporate the different frequency regulation services defined by systems operators [13], the frequency regulation capability of grid-forming converters [14], wind turbines [15], and flywheel energy storage [16], as well as the effect of considering multiple regions with different levels of inertia [17]. In general, these works are based on adding frequency-constraints to the UC model, such that large frequency excursions resulting from generator outages are avoided, as these are relatively common in bulk-power systems with a large number of generators. However, none of these works consider the impact of second-to-second renewable power fluctuations on the system's frequency regulation performance, instead focusing exclusively on frequency excursions caused by outages. Furthermore, these papers focus on bulk-power systems, which significantly differ from isolated microgrids, particularly with respect to frequency stability and control [6].

Based on the aforementioned discussion, the present paper extends [12] by further incorporating the impact of second-to-second power fluctuations on transient frequency dynamics. This results on a frequency-constrained EMS model capable of guaranteeing an adequate frequency regulation performance in accordance with modern DER operating standards (e.g., [18]). Thus, the main objectives and contributions of this paper can be summarized as follows:

- Accurate linear equations describing frequency excursions and Rate-of-Change-of-Frequency (RoCoF) values in the presence of second-to-second power imbalances are developed, which then serve as a basis for the design of a computationally efficient microgrid EMS model with frequency and RoCoF limit constraints suitable for near real-time practical applications.
- Exhaustive transient simulations on a realistic test system using thoroughly validated frequency dynamic and control models are presented to demonstrate the modeling accuracy of the proposed EMS and the benefits resulting from its implementation in isolated microgrids. Such benefits include the reduction of total operating cost while keeping an adequate frequency regulation performance compliant with modern DER operating standards.

The rest of the paper is organized as follows: Section II presents the theoretical background required for modeling short-term power fluctuations, reserves, battery degradation, and frequency regulation. Section III discusses the design of the proposed frequency-constrained EMS model, for which novel mathematical expressions describing the impact of second-to-second power imbalances on microgrid operation and frequency dynamics are developed. Section IV presents computational experiments and results, demonstrating the relevance and advantages of the proposed model. Finally, Section V presents the main conclusions of the paper.

II. Theoretical Background

In this section, previously existing models that are used in this paper are discussed. First, the models needed for the design of the proposed EMS are presented, namely, short-term power fluctuations, system reserve needs, and battery degradation models. Then, dynamic and control models used to describe the frequency regulation of the microgrid and perform transient simulations are described.

A. Short-term Power Fluctuations Modeling

Within the context of optimal dispatch models, second-to-second power fluctuations can be modeled by considering two different time-frames, as in [12]: one for long dispatch time intervals $h \in \mathcal{H} = \{1, \dots, H\}$, and another for short time intervals $j \in \mathcal{J} = \{1, \dots, J\}$. Accordingly, any generic instantaneous power vector $\boldsymbol{p}_h$ during dispatch time interval h can be split into long and short term components as follows:

$$\boldsymbol{p}_h = \underbrace{[\hat{p}_h + \chi_h(\xi)]}_{\text{long term}} \mathbf{1} + \underbrace{\boldsymbol{r}_h(\xi)}_{\text{short term}} \tag{1}$$

where $\boldsymbol{p}_h = [p_{h,1}, \dots, p_{h,j}, \dots, p_{h,J}]$; $\mathbf{1}$ is a vector of ones of dimension J; $\hat{p}_h$ is the forecast average power; χ_h is the average power's forecast error, which is affected by uncertainty ξ; and $\boldsymbol{r}_h = [r_{h,1}, \dots, r_{h,j}, \dots, r_{h,J}]$ represents the short-term fluctuations, which are also affected by uncertainty. Note

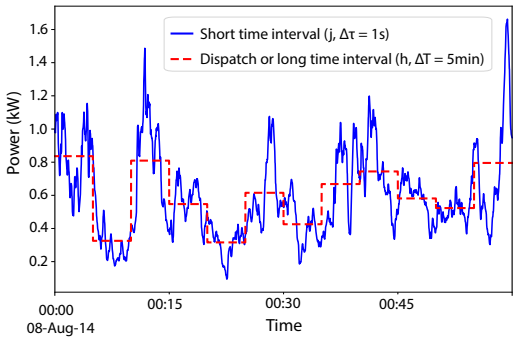


Fig. 1. Average powers and intra-dispatch fluctuations for a 10 kW wind plant at the KLFN microgrid [12].

that scalars $\hat{p}_h$ and χ_h are constant during dispatch time interval h, and thus have a time resolution of ΔT_h. In contrast, $\boldsymbol{r}_h$ varies in accordance with the short time interval index j, and thus has a time-step $\Delta\tau \ll \Delta T_h$. An illustrative example of this modeling approach is depicted in Fig. 1, where measurements from the Kasabonika Lake First Nation (KLFN) microgrid extracted from [19], with a time resolution of $\Delta\tau$ = 1s, are used to define: (i) average powers $\hat{p}_h$, which remain constant during the long dispatch time intervals with length ΔT_h = 5min $\forall h \in \mathcal{H}$; and (ii) short-term fluctuations $\boldsymbol{r}_h$, which oscillate around such average powers. Note that in this example, forecast errors are not present, i.e., $\chi_h = 0 \ \forall h \in \mathcal{H}$.

Based on framework (1), it can be noted that conventional EMS models such as [1]–[3] focus exclusively on modeling the forecast average power $\hat{p}_h$ and its associated forecast error χ_h, neglecting short-term fluctuations $\boldsymbol{r}_h$. In contrast, modern EMS incorporating short-term power fluctuations characterize $\boldsymbol{r}_h$ either directly, by adding short time intervals $j \in \mathcal{J}$ in the model (e.g., [9]–[11]), or by using an alternative low-order representation of $\boldsymbol{r}_h$ for computational efficiency [12]. Hence, second-to-second power fluctuations are modeled using the latter approach, as computational tractability plays a fundamental role in near real-time practical applications. Specifically, here short-term fluctuations $\boldsymbol{r}_h$ are described by its feature-based representation:

$$\boldsymbol{v}_h = \left[\text{std}(\boldsymbol{r}_h),\ \text{tae}(\boldsymbol{r}_h)\right] \tag{2}$$

where std$(\cdot)$ and tae$(\cdot)$ are the standard deviation and truncated absolute expectation operators, respectively; and $\boldsymbol{v}_h$ is a vector of dimension equal to 2, which is significantly lower than $J = \dim(\boldsymbol{r}_h)$. The details regarding the tae$(\cdot)$ operator are discussed in Section III-B.

B. Reserves Modeling

Based on (1), reserves are needed for handling uncertain forecast errors and short-term fluctuations, which are described next as per [12]. Thus, the forecast error reserve need ζ_h^{χ} at dispatch time interval h can be defined using the microgrid's net load forecast error χ_h^{MG}, as follows:

$$\chi_h^{MG}(\xi) = \hat{D}_h\,\tilde{\chi}_h^{D}(\xi) - \hat{p}_h^{W}\,\tilde{\chi}_h^{W}(\xi) - \hat{p}_h^{S}\,\tilde{\chi}_h^{S}(\xi) \tag{3a}$$

$$\text{std}\left(\chi_h^{MG}\right)^2 = \left(\hat{D}_h\tilde{\sigma}_h^{\chi,D}\right)^2 + \left(\hat{p}_h^{W}\tilde{\sigma}_h^{\chi,W}\right)^2 + \left(\hat{p}_h^{S}\tilde{\sigma}_h^{\chi,S}\right)^2 \tag{3b}$$

$$\zeta_h^{\chi} = \epsilon_{\chi}\,\text{std}\left(\chi_h^{MG}\right) \tag{3c}$$

where $\hat{D}_h$, $\hat{p}_h^W$, and $\hat{p}_h^S$ are the forecast average powers corresponding to demand, wind generation, and solar generation, respectively; $\tilde{\chi}_h^D$, $\tilde{\chi}_h^W$, and $\tilde{\chi}_h^S$ are normalized zero-mean random scalars representing the errors associated with each forecast; $\tilde{\sigma}_h^{\chi,D} = \text{std}\left(\tilde{\chi}_h^D\right)$, $\tilde{\sigma}_h^{\chi,W} = \text{std}\left(\tilde{\chi}_h^W\right)$, and $\tilde{\sigma}_h^{\chi,S} = \text{std}\left(\tilde{\chi}_h^S\right)$ are sample standard deviations estimated from normalized historical samples of forecast errors $\chi_h^D/\hat{D}_h$, $\chi_h^W/\hat{p}_h^W$, and $\chi_h^S/\hat{p}_h^S$, respectively; and ϵ_{χ} is a parameter to adjust the desired confidence level.

Similarly, the regulation reserve need $\zeta_h^{\boldsymbol{r}}$ at dispatch time interval h can be defined using the microgrid's regulation signal $\boldsymbol{r}_h^{MG}$, as follows:

$$\boldsymbol{r}_h^{MG}(\xi) = \hat{D}_h\,\tilde{\boldsymbol{r}}_h^{D}(\xi) - \hat{p}_h^{W}\,\tilde{\boldsymbol{r}}_h^{W}(\xi) - \hat{p}_h^{S}\,\tilde{\boldsymbol{r}}_h^{S}(\xi) \tag{4a}$$

$$\text{std}\left(\boldsymbol{r}_h^{MG}\right)^2 = \left(\hat{D}_h\tilde{\sigma}_h^{\boldsymbol{r},D}\right)^2 + \left(\hat{p}_h^{W}\tilde{\sigma}_h^{\boldsymbol{r},W}\right)^2 + \left(\hat{p}_h^{S}\tilde{\sigma}_h^{\boldsymbol{r},S}\right)^2 \tag{4b}$$

$$\zeta_h^{\boldsymbol{r}} = \epsilon_{\boldsymbol{r}}\,\text{std}\left(\boldsymbol{r}_h^{MG}\right) \tag{4c}$$

where $\tilde{\boldsymbol{r}}_h^D$, $\tilde{\boldsymbol{r}}_h^W$, and $\tilde{\boldsymbol{r}}_h^S$ are zero-mean random vectors representing the normalized intra-dispatch fluctuations stemming from demand, wind generation, and solar generation; $\tilde{\sigma}_h^{\boldsymbol{r},D} = \text{std}\left(\tilde{\boldsymbol{r}}_h^D\right)$, $\tilde{\sigma}_h^{\boldsymbol{r},W} = \text{std}\left(\tilde{\boldsymbol{r}}_h^W\right)$, and $\tilde{\sigma}_h^{\boldsymbol{r},S} = \text{std}\left(\tilde{\boldsymbol{r}}_h^S\right)$ are the sample standard deviations; and $\epsilon_{\boldsymbol{r}}$ is a parameter to adjust the desired confidence level. Note that unlike the case for forecast error reserve in (3), standard deviations are computed in (4) by concatenating normalized historical samples of $r_{j,h}^D/\hat{D}_h$, $r_{j,h}^W/\hat{p}_h^W$, and $r_{j,h}^S/\hat{p}_h^S$, since $\tilde{\boldsymbol{r}}$ is a random vector of dimension J. Furthermore, observe that standard deviations $\tilde{\sigma}_h^{\boldsymbol{r}}$ only depend on dispatch time interval $h \in \mathcal{H}$, since the short time interval index $j \in \mathcal{J}$ is avoided in accordance with the feature-based representation in (2).

C. Battery Degradation Modeling

Modern EMS models consider battery degradation, as it plays a significant role when determining total operating costs. Here, the approach in [12] is followed, where the degradation resulting from the repeated charging and discharging of battery $b \in \mathcal{B}$ is modeled through a computationally efficient piecewise linear degradation model, for which the battery's cycle depth range is split into even partitions $l \in \mathcal{L}$, as follows:

$$f_b^{\Phi}(\boldsymbol{c},\boldsymbol{d}) = \frac{\hat{\phi}_{b,l}}{2}\frac{\Delta t}{E_b}\sum_{t\in\mathcal{T}}\sum_{l\in\mathcal{L}}\left(\eta_b^C\,c_{b,l,t} + \frac{d_{b,l,t}}{\eta_b^D}\right) \tag{5a}$$

$$s_{b,l,t} - s_{b,l,t-1} = \frac{\Delta t}{E_b}\left(\eta_b^C\,c_{b,l,t} - \frac{d_{b,l,t}}{\eta_b^D}\right) \tag{5b}$$

$$0 \le s_{b,l,t} \le \overline{S}_{b,l} \quad \forall b \in \mathcal{B}, l \in \mathcal{L}, t \in \mathcal{T} \tag{5c}$$

where $f_b^{\Phi}(\cdot) \in [0,1]$ is the battery's b accumulated degradation; $\mathcal{T}$ is a set of generic time intervals t with time-step length Δt;

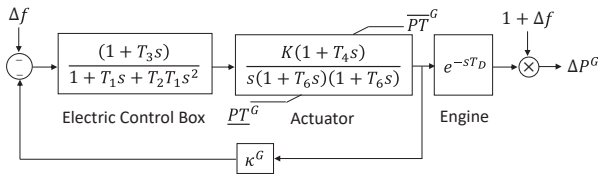


Fig. 2. Block diagram of diesel generator governor model (DEGOV1) [20].

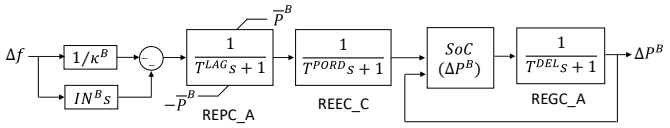


Fig. 3. Block diagram of battery frequency response model [21].

$c_{b,l,t}$ and $d_{b,l,t}$ are the charging and discharging of battery's b partition l at time t; $s_{b,l,t}$ is the State-of-Charge (SoC) of battery's b partition l; E_b, η_b^C, and η_b^D are the battery's energy capacity, charging efficiency, and discharging efficiency; and $\hat{\phi}_{b,l}$ is the piecewise linear degradation coefficient. Observe that partition l of battery b has its own SoC $s_{b,l,t}$, which is bounded by the partition's depth range $\overline{S}_{b,l}$.

D. Frequency Regulation Modeling

As previously discussed, this paper aims to incorporate frequency regulation and its dynamics within the context of EMS models for isolated microgrids. Thus, frequency dynamic models for diesel generators and batteries, as well as load shedding and renewable curtailment controllers, are considered here. Such models are based on a frequency-droop control, as this is the common approach used in isolated microgrids.

Diesel Generators (G) are modeled using the diesel engine governor DEGOV1 model depicted in Fig. 2 [20], where Δf is the frequency deviation, $\overline{PT}^G$ and $\underline{PT}^G$ are the generator's maximum and minimum torque, and κ^G is the the generator's frequency droop. Note that in this and following figures, T and K are used to represent controller time delays and gains, respectively. Batteries (B) are modeled based on WECC's generic modules REPC_A, REEC_C, REGC_A [21], which have been simplified to represent only frequency dynamics and controllers' time delays, as illustrated in Fig. 3. The battery dynamic model includes maximum power capacity $\overline{P}^B$, frequency droop κ^B, virtual inertia coefficient IN^B, and SoC limit function $SoC\left(\Delta P^B\right)$, which automatically stops the battery's charging (discharging) if the upper (lower) SoC limit is reached.

Auxiliary Load Shedding (LS) and Renewable Curtailment (RC) controllers are also modeled, which are designed to prevent system collapse in the presence of unexpectedly large and fast power fluctuations. In particular, linear percentage-based LS and RC controllers are considered here, which are illustrated in Fig. 4 and Fig. 5, respectively. Note that these controllers are triggered if the upper (or lower) frequency deviation limits $\pm\overline{\Delta f}$ are reached, in accordance with typical DER operating standards [18]. Furthermore, observe that both controllers have damped percentage gains, which depend on

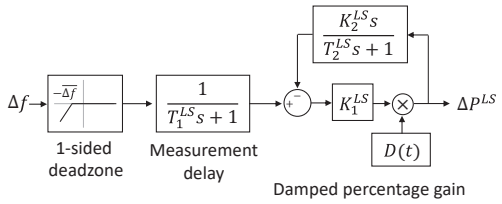


Fig. 4. Block diagram of load shedding frequency control scheme.

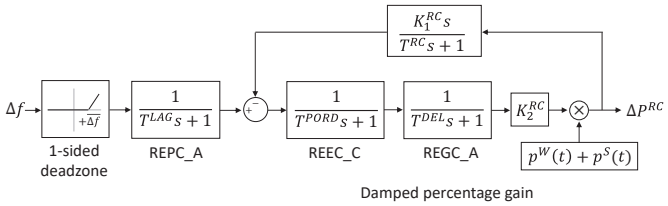


Fig. 5. Block diagram of renewable curtailment frequency control scheme.

the instantaneous demand $D(t)$, wind generation $p^W(t)$, and solar generation $p^S(t)$ at time t.

To further enhance the microgrid's frequency regulation, a proportional Voltage Frequency Controller (VFC) installed on the diesel generators is also considered [22]. The dynamic model associated with the VFC is presented in Fig. 6, which exploits the voltage sensitivity of loads K^{PV}, and has a proportional gain K^{VFC} and voltage deviation limit $\overline{\Delta V}$. Note that for simplicity, the generator's voltage dynamics are represented by a 4th order transfer function $V^G(s)$, which is estimated using MATLAB's `frestimate` fitting function based on the response of a 6^{th} order Synchronous Machine (SM) and an AC1A exciter to small voltage reference perturbations.

Using the aforementioned dynamic models, the microgrid's frequency regulation model can be described by its Center of Inertia (CoI) [13]–[17], as illustrated in Fig. 7. In the figure, $r^D(t), r^W(t)$ and $r^S(t)$ are continuous-time functions representing the short-term fluctuations of demand, wind generation, and solar generation, respectively; IN^{MG} is the total synchronous inertia provided by the diesel generators; K^{PF} is the frequency sensitivity of loads; and ΔP is the total power change resulting from short-term fluctuations and frequency regulation.

III. Energy Management System Model

In this section, the design of the proposed frequency-constrained EMS model is discussed. This includes the equations and constraints used to build the UC model for determining the EMS dispatch decisions, as well as the general architecture required for its implementation.

A. Capacity and Reserve Constraints

As discussed in Section II, forecast error and regulation reserves are needed for the reliable operation of isolated microgrids. Thus, enough slack power capacity should be allocated to generators $g \in \mathcal{G}$ such that the required reserves

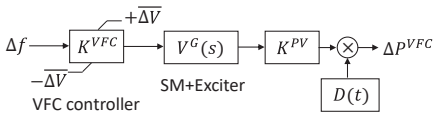


Fig. 6. Block diagram of a proportional Voltage Frequency Controller [22].

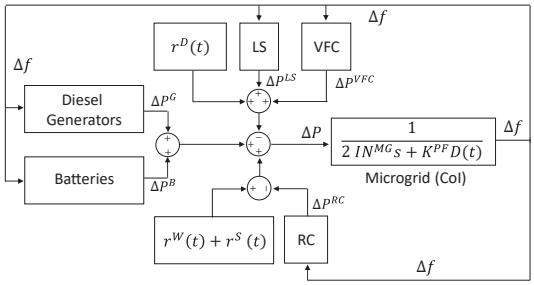


Fig. 7. Microgrid's frequency regulation model.

are available when needed. This is described by the following generator power capacity constraints $\forall g \in \mathcal{G}$:

$$\hat{p}^G_{g,h} + \Delta p^{G,\chi,\uparrow}_{g,h} \leq \overline{P}^G_g\, u_{g,h} \quad \forall h \in \mathcal{H}^{\boldsymbol{r}} \quad (6a)$$
$$\hat{p}^G_{g,h} - \Delta p^{G,\chi,\downarrow}_{g,h} \geq \underline{P}^G_g u_{g,h} \quad \forall h \in \mathcal{H}^{\boldsymbol{r}} \quad (6b)$$
$$\hat{p}^G_{g,h} + \Delta p^{G,\chi,\uparrow}_{g,h} + \Delta p^{G,\boldsymbol{r},\uparrow}_{g,h} \leq \overline{PT}^G_g\, u_{g,h} \quad \forall h \in \mathcal{H}^{\boldsymbol{r}} \quad (6c)$$
$$\hat{p}^G_{g,h} - \Delta p^{G,\chi,\downarrow}_{g,h} - \Delta p^{G,\boldsymbol{r},\downarrow}_{g,h} \geq \underline{PT}^G_g\, u_{g,h} \quad \forall h \in \mathcal{H}^{\boldsymbol{r}} \quad (6d)$$
$$\hat{p}^G_{g,h} + \Delta p^{G,\chi,\uparrow}_{g,h} + \Delta p^{G,\boldsymbol{r},\uparrow}_{g,h} \leq \overline{P}^G_g\, u_{g,h} \quad \forall h \in \mathcal{H} \setminus \mathcal{H}^{\boldsymbol{r}} \quad (6e)$$
$$\hat{p}^G_{g,h} - \Delta p^{G,\chi,\downarrow}_{g,h} - \Delta p^{G,\boldsymbol{r},\downarrow}_{g,h} \geq \underline{P}^G_g\, u_{g,h} \quad \forall h \in \mathcal{H} \setminus \mathcal{H}^{\boldsymbol{r}} \quad (6f)$$

where $\hat{p}^G_{g,h}$ denotes the generation set-point or average power of generator g during dispatch time interval h; $\Delta p^{G,\chi,\uparrow/\downarrow}_{g,h}$ is the upward ($\uparrow$)/downward ($\downarrow$) forecast error reserve provided by generator g; $\Delta p^{G,\boldsymbol{r},\uparrow/\downarrow}_{g,h}$ is the upward/downward regulation reserve provided by generator g; $u_{g,h}$ is a binary variable indicating the generator's ON/OFF status; $\overline{P}^G_g$ and $\underline{P}^G_g$ are generator g's steady-state maximum and minimum power; and $\overline{PT}^G_g$ and $\underline{PT}^G_g$ are generator g's transient maximum and minimum power, as per Fig. 2, with $\overline{PT}^G_g \geq \overline{P}^G_g$ and $\underline{PT}^G_g \leq \underline{P}^G_g$. Note that (6a)-(6d) are defined for the first $\mathcal{H}^{\boldsymbol{r}} \subset \mathcal{H}$ dispatch time intervals, whereas (6e)-(6f) are defined for the remaining dispatch time intervals resulting from the set difference $\mathcal{H} \setminus \mathcal{H}^{\boldsymbol{r}}$. This distinction is related to the use of growing time steps in EMSs based on a Model Predictive Control (MPC) [1]–[3], [12], for which a finer time resolution is used at the first time steps.

Note that (6) extends [12] by considering transient power capacity limits in addition to the conventional steady-steady power capacity limits. This modeling approach is based on the fact that for diesel generators, steady-state power capacity limits can be temporarily violated for a few seconds [20]. Thus, additional slack capacities $\overline{PT}^G_g - \overline{P}^G_g \geq 0$ and $\underline{P}^G_g - \underline{PT}^G_g \geq 0$ are considered for the regulation reserve, as this reserve is only fully deployed for a few seconds in practice.

Similar to the case of generators, power capacity limits are also considered for batteries, which can be described as follows $\forall b \in \mathcal{B}, h \in \mathcal{H}$:

$$\sum_{l \in \mathcal{L}} \left(c_{b,l,h} + \Delta p^{B,C,\chi,\downarrow}_{b,l,h} + \Delta p^{B,C,\boldsymbol{r},\downarrow}_{b,l,h} \right) \leq \overline{P}^B_b \quad (7a)$$
$$\sum_{l \in \mathcal{L}} \left(d_{b,l,h} + \Delta p^{B,D,\chi,\uparrow}_{b,l,h} + \Delta p^{B,D,\boldsymbol{r},\uparrow}_{b,l,h} \right) \leq \overline{P}^B_b \quad (7b)$$

where battery b is partitioned into even segments $l \in \mathcal{L}$, as per (5). Accordingly, $c_{b,l,h}$ and $d_{b,l,h}$ are the charging and discharging set-points of battery's b partition l during dispatch time interval h; $\Delta p^{B,C,\chi,\downarrow}_{b,l,h}$ and $\Delta p^{B,C,\boldsymbol{r},\downarrow}_{b,l,h}$ are, respectively, the downward forecast error and regulation reserves provided by increasing the battery's charging (C); $\Delta p^{B,D,\chi,\uparrow}_{b,l,h}$ and $\Delta p^{B,D,\boldsymbol{r},\uparrow}_{b,l,h}$ are, respectively, the upward forecast error and regulation reserves provided by increasing the battery's discharging (D); and $\overline{P}^B_b$ is battery b's maximum power capacity, as per Fig. 3. Note that in this case steady-state and transient capacity limits are equal, as both are equally constrained by the battery converter's capabilities [21].

Unlike [12], additional battery slack capacity resulting from reducing charging and discharging is also considered here for reserve provision [23], as follows $\forall b \in \mathcal{B}, l \in \mathcal{L}, h \in \mathcal{H}$:

$$\Delta p^{B,C,\chi,\uparrow}_{b,l,h} + \Delta p^{B,C,\boldsymbol{r},\uparrow}_{b,l,h} \leq c_{b,l,h} \quad (8a)$$
$$\Delta p^{B,D,\chi,\downarrow}_{b,l,h} + \Delta p^{B,D,\boldsymbol{r},\downarrow}_{b,l,h} \leq d_{b,l,h} \quad (8b)$$

where $\Delta p^{B,C,\chi,\uparrow}_{b,l,h}$ and $\Delta p^{B,C,\boldsymbol{r},\uparrow}_{b,l,h}$ are the upward forecast error and regulation reserves provided by decreasing the battery's charging; and $\Delta p^{B,D,\chi,\downarrow}_{b,l,h}$ and $\Delta p^{B,D,\boldsymbol{r},\downarrow}_{b,l,h}$ are the downward forecast error and regulation reserves provided by decreasing the battery's discharging, respectively. Furthermore, constraints to ensure enough energy is saved for battery reserve provision are adapted from [12], as follows $\forall b \in \mathcal{B}, l \in \mathcal{L}, h \in \mathcal{H}$:

$$s_{b,l,h-1} + \frac{\Delta T_h\, \eta^C_b}{E_b} \left(c_{b,l,h} + \Delta p^{B,C,\chi,\downarrow}_{b,l,h} + \frac{1}{2} \Delta p^{B,C,\boldsymbol{r},\downarrow}_{b,l,h} \right) - \frac{\Delta T_h}{E_b\, \eta^D_b} \left(d_{b,l,h} - \Delta p^{B,D,\chi,\downarrow}_{b,l,h} - \frac{1}{2} \Delta p^{B,D,\boldsymbol{r},\downarrow}_{b,l,h} \right) \leq \overline{S}_{b,l} \quad (9a)$$

$$s_{b,l,h-1} - \frac{\Delta T_h}{E_b\, \eta^D_b} \left(d_{b,l,h} + \Delta p^{B,D,\chi,\uparrow}_{b,l,h} + \frac{1}{2} \Delta p^{B,D,\boldsymbol{r},\uparrow}_{b,l,h} \right) + \frac{\Delta T_h\, \eta^C_b}{E_b} \left(c_{b,l,h} - \Delta p^{B,C,\chi,\uparrow}_{b,l,h} - \frac{1}{2} \Delta p^{B,C,\boldsymbol{r},\uparrow}_{b,l,h} \right) \geq 0 \quad (9b)$$

where the worst-case scenario for energy requirement is assumed. Note that this formulation differs from [12] in two aspects. First, additional battery slack capacities resulting from reduced (dis)charging are incorporated here, as per (8). Second, regulation reserves $\Delta p^{\boldsymbol{r}}$ include a $1/2$ term, since upward (downward) regulation reserves are assumed to be deployed at full capacity at most for half of the dispatch time interval length ΔT_h, based on the zero-mean characteristic of $\boldsymbol{r}$ in (1).

Based on (6)-(8), the forecast error reserve balance can be represented as follows $\forall h \in \mathcal{H}$:

$$\zeta_h^{\chi} = \sum_{g\in\mathcal{G}} \Delta p_{g,h}^{G,\chi,\uparrow/\downarrow} + \sum_{b\in\mathcal{B}}\sum_{l\in\mathcal{L}} \left(\Delta p_{b,l,h}^{B,D,\chi,\uparrow/\downarrow} + \Delta p_{b,l,h}^{B,C,\chi,\uparrow/\downarrow}\right) \tag{10}$$

Similarly, the regulation reserve balance can be represented as follows:

$$\begin{aligned}\zeta_h^{\boldsymbol{r}} =& \sum_{g\in\mathcal{G}} \Delta p_{g,h}^{G,\boldsymbol{r},\uparrow/\downarrow} + \sum_{b\in\mathcal{B}}\sum_{l\in\mathcal{L}} \left(\Delta p_{b,l,h}^{B,D,\boldsymbol{r},\uparrow/\downarrow} + \Delta p_{b,l,h}^{B,C,\boldsymbol{r},\uparrow/\downarrow}\right) \\ &+ \Delta p_h^{PF,\boldsymbol{r},\uparrow/\downarrow} + \Delta p_h^{VFC,\boldsymbol{r},\uparrow/\downarrow} \quad \forall h \in \mathcal{H}^{\boldsymbol{r}} \qquad (11a)\\ \zeta_h^{\boldsymbol{r}} =& \sum_{g\in\mathcal{G}} \Delta p_{g,h}^{G,\boldsymbol{r},\uparrow/\downarrow} + \sum_{b\in\mathcal{B}}\sum_{l\in\mathcal{L}} \left(\Delta p_{b,l,h}^{B,D,\boldsymbol{r},\uparrow/\downarrow} + \Delta p_{b,l,h}^{B,C,\boldsymbol{r},\uparrow/\downarrow}\right) \\ &\forall h \in \mathcal{H} \setminus \mathcal{H}^{\boldsymbol{r}} \qquad (11b)\end{aligned}$$

where (11a) includes the additional regulation capabilities $\Delta p_h^{PF,\boldsymbol{r},\uparrow/\downarrow}$ and $\Delta p_h^{VFC,\boldsymbol{r},\uparrow/\downarrow}$ stemming from frequency sensitive loads and VFCs, respectively. The constraints associated with these two variables are discussed in Section III-C.

B. Operational Impact of Reserve Provision

Forecast error and regulation reserves are continuously being deployed to handle real-time mismatches, and thus have an impact on the instantaneous power outputs of the microgrid's generators and batteries. Accordingly, the allocation of forecast error and regulation reserves influence the expected average thermal generation, battery SoC, and battery degradation. This effect can be modelled using the Expected Reserve Utilization (ERU), which quantifies how much of the allocated reserve is expected to be deployed on average. In [12], the ERU is computed using the mean absolute deviation (mad) of power imbalances. Here, the mad is replaced by the tae$(\cdot)$ operator, which has an improved accuracy and can be defined as follows:

$$\begin{aligned}\text{tae}(Z,\zeta) =& \int_{-\zeta}^{\zeta} |z| f(z) dz \\ &+ \zeta\left[\int_{-\infty}^{-\zeta} f(z)dz + \int_{\zeta}^{\infty} f(z)dz\right] \qquad (12)\end{aligned}$$

where Z is a random variable representing uncertain power imbalances, $f(z)$ is its associated probability density function, and ζ is the available reserve capacity. Note that this formulation closely resembles $\text{mad}(Z) = \mathbb{E}(|Z|)$, but with the difference that $f(z)$ is truncated for $|z| \geq \zeta$, and the corresponding truncated values are clustered at $z = \pm\zeta$. This alternative definition is motivated by how reserves are deployed in practice, since if insufficient reserves are available, i.e., $|z| \geq \zeta$, only a reserve equal to $\pm\zeta$ will be deployed.

Based on (2)-(4) and (12), the ERU of the forecast error and regulation reserves can be computed as follows:

$$\varphi_h^{\chi} = \text{tae}\left(\chi_h^{MG}, \zeta_h^{\chi}\right)/\zeta_h^{\chi}, \quad \varphi_h^{\boldsymbol{r}} = \text{tae}\left(\boldsymbol{r}_h^{MG}, \zeta_h^{\boldsymbol{r}}\right)/\zeta_h^{\boldsymbol{r}} \tag{13}$$

Assuming that both χ_h^{MG} and $\boldsymbol{r}_h^{MG}$ resemble a normal distribution, and replacing (3c) and (4c), one has that:

$$\varphi_h^{\chi/\boldsymbol{r}} = \frac{1}{\epsilon_{\chi/\boldsymbol{r}}}\sqrt{\frac{2}{\pi}}\left[1 - \exp\left(-\frac{\epsilon_{\chi/\boldsymbol{r}}^2}{2}\right)\right] + 1 - \text{erf}\left(\frac{\epsilon_{\chi/\boldsymbol{r}}}{\sqrt{2}}\right) \tag{14}$$

where exp and erf are the exponential and Gauss error functions, respectively.

Based on (14), the change in the expected average power of generators $\Delta e_{g,h}$, battery's SoC $\Delta s_{b,l,h}$, and battery degradation $\Delta\phi_{b,l,h}$ due to the reserve provision can be adapted from [12], as follows:

$$\begin{aligned}\Delta e_{g,h} =& \frac{\varphi_h^{\chi}}{2}\left(\Delta p_{g,h}^{G,\chi,\uparrow} - \Delta p_{g,h}^{G,\chi,\downarrow}\right) \\ &+ \frac{\varphi_h^{\boldsymbol{r}}}{2}\left(\Delta p_{g,h}^{G,\boldsymbol{r},\uparrow} - \Delta p_{g,h}^{G,\boldsymbol{r},\downarrow}\right) \qquad (15)\\ \Delta s_{b,l,h} =& \frac{\varphi_h^{\chi}}{2}\frac{\Delta T_h}{E_b}\eta_b^C\left(\Delta p_{b,l,h}^{B,C,\chi,\downarrow} - \Delta p_{b,l,h}^{B,C,\chi,\uparrow}\right) \\ &- \frac{\varphi_h^{\chi}}{2}\frac{\Delta T_h}{E_b}\frac{1}{\eta_b^D}\left(\Delta p_{b,l,h}^{B,D,\chi,\uparrow} - \Delta p_{b,l,h}^{B,D,\chi,\downarrow}\right) \\ &+ \frac{\varphi_h^{\boldsymbol{r}}}{2}\frac{\Delta T_h}{E_b}\eta_b^C\left(\Delta p_{b,l,h}^{B,C,\boldsymbol{r},\downarrow} - \Delta p_{b,l,h}^{B,C,\boldsymbol{r},\uparrow}\right) \\ &- \frac{\varphi_h^{\boldsymbol{r}}}{2}\frac{\Delta T_h}{E_b}\frac{1}{\eta_b^D}\left(\Delta p_{b,l,h}^{B,D,\boldsymbol{r},\uparrow} - \Delta p_{b,l,h}^{B,D,\boldsymbol{r},\downarrow}\right) \qquad (16)\\ \Delta\phi_{b,l,h} =& \frac{\hat{\phi}_{b,l}}{2}\frac{\varphi_h^{\chi}}{2}\frac{\Delta T_h}{E_b}\eta_b^C\left(\Delta p_{b,l,h}^{B,C,\chi,\downarrow} - \Delta p_{b,l,h}^{B,C,\chi,\uparrow}\right) \\ &+ \frac{\hat{\phi}_{b,l}}{2}\frac{\varphi_h^{\chi}}{2}\frac{\Delta T_h}{E_b}\frac{1}{\eta_b^D}\left(\Delta p_{b,l,h}^{B,D,\chi,\uparrow} - \Delta p_{b,l,h}^{B,D,\chi,\downarrow}\right) \\ &+ \frac{\hat{\phi}_{b,l}}{2}\frac{\varphi_h^{\boldsymbol{r}}}{2}\frac{\Delta T_h}{E_b}\eta_b^C\left(\Delta p_{b,l,h}^{B,C,\boldsymbol{r},\downarrow} - \Delta p_{b,l,h}^{B,C,\boldsymbol{r},\uparrow}\right) \\ &+ \frac{\hat{\phi}_{b,l}}{2}\frac{\varphi_h^{\boldsymbol{r}}}{2}\frac{\Delta T_h}{E_b}\frac{1}{\eta_b^D}\left(\Delta p_{b,l,h}^{B,D,\boldsymbol{r},\uparrow} - \Delta p_{b,l,h}^{B,D,\boldsymbol{r},\downarrow}\right) \qquad (17)\end{aligned}$$

Note that unlike [12], and similar to (9), additional battery slack capacities resulting from reduced (dis)charging are incorporated, and a $1/2$ term is included for regulation reserves.

Based on (16), the expected SoC at the end of dispatch time interval h, resulting from the provision of energy shifting and reserve services, can be obtained as follows:

$$s_{b,l,h} - s_{b,l,h-1} = \frac{\Delta T_h}{E_b}\left(\eta_b^C\, c_{b,l,h} - \frac{d_{b,l,h}}{\eta_b^D}\right) + \Delta s_{b,l,h} \tag{18}$$

$$0 \leq s_{b,l,h} \leq \overline{S}_{b,l} \quad \forall b \in \mathcal{B}, l \in \mathcal{L}, h \in \mathcal{H} \tag{19}$$

Similarly, based on (17), the total battery degradation resulting from the provision of energy shifting and reserve services can be obtained as follows:

$$\Phi_{b,l,h} = \frac{\hat{\phi}_{b,l}}{2}\frac{\Delta T_h}{E_b}\left(\eta_b^C\, c_{b,l,h} + \frac{d_{b,l,h}}{\eta_b^D}\right) + \Delta\phi_{b,l,h} \tag{20}$$

C. Frequency-Dynamics Constraints

Unlike previous works on microgrid EMS, explicit frequency constraints are considered here, such that an adequate frequency regulation performance is ensured in daily microgrid

operations. In the case of thermal generators, their maximum deliverable short-term regulation is defined by their frequency-droop κ_g^G, and the maximum frequency deviation limit $\overline{\Delta f}$ imposed by DER operating standards [18], yielding the following constraint:

$$\Delta p_{g,h}^{G,\boldsymbol{r},\uparrow/\downarrow} \leq \frac{\overline{\Delta f}}{f_0} \frac{\overline{P}_g^G}{\kappa_g^G} \quad \forall g \in \mathcal{G}, h \in \mathcal{H}^{\boldsymbol{r}} \tag{21}$$

where f_0 is the microgrid's nominal frequency in Hz. Similarly, for batteries, the maximum deliverable short-term regulation is given by the following constraints $\forall b \in \mathcal{B}, h \in \mathcal{H}^{\boldsymbol{r}}$:

$$\sum_{l \in \mathcal{L}} \left(\Delta p_{b,l,h}^{B,D,\boldsymbol{r},\uparrow} + \Delta p_{b,l,h}^{B,C,\boldsymbol{r},\uparrow} \right) \leq \frac{\overline{\Delta f}}{f_0} \frac{\overline{P}_b^B}{\kappa_b^B} \tag{22a}$$

$$\sum_{l \in \mathcal{L}} \left(\Delta p_{b,l,h}^{B,C,\boldsymbol{r},\downarrow} + \Delta p_{b,l,h}^{B,D,\boldsymbol{r},\downarrow} \right) \leq \frac{\overline{\Delta f}}{f_0} \frac{\overline{P}_b^B}{\kappa_b^B} \tag{22b}$$

where κ_b^B is the battery's frequency droop.

Loads provide a damping factor stemming from their frequency sensitivity K^{PF} (see Fig. 7). This feature is modeled in reserve regulation balance (11a) through variable $\Delta p_h^{PF,\boldsymbol{r},\uparrow/\downarrow}$, which is constrained as follows $\forall h \in \mathcal{H}^{\boldsymbol{r}}$:

$$\Delta p_h^{PF,\boldsymbol{r},\uparrow/\downarrow} \leq \frac{\overline{\Delta f}}{f_0} K^{PF} \left(\hat{D}_h - ls_h \right) \tag{23}$$

where ls_h is the scheduled load shedding during dispatch time interval h. Loads also present a voltage sensitivity K^{PV}, which can be exploited to provide additional frequency damping through the inclusion of VFCs in diesel generators (see Fig. 6). This additional flexibility is incorporated in (11a) through variable $\Delta p_h^{VFC,\boldsymbol{r},\uparrow/\downarrow}$, which is constrained as follows $\forall h \in \mathcal{H}^{\boldsymbol{r}}$:

$$\Delta p_h^{VFC,\boldsymbol{r},\uparrow/\downarrow} \leq \frac{\overline{\Delta f}}{f_0} K^{VFC} K^{PV} \left(\hat{D}_h - ls_h \right) \tag{24}$$

Another relevant aspect to consider in microgrid frequency regulation is the RoCoF limit imposed by DER operating standards [18], since excessively large RoCoF values might lead to operating issues such as loss of synchronism in converters' phase locked loops [6]. Accordingly, a RoCoF constraint is also considered here, which is derived using the CoI frequency dynamic equation (see Fig. 7). Hence, taking into account that automatic frequency controllers have an inherent time delay and thus are not immediately available, the instantaneous frequency deviation resulting from short-term power fluctuations can be described by:

$$2IN^{MG} \frac{d\Delta f}{dt} + K^{PF} D(t) \Delta f = r^W(t) + r^S(t) - r^D(t). \tag{25}$$

Thus, neglecting load damping K^{PF}, as in [13], one can obtain the following overestimation for the instantaneous RoCoF:

$$RoCoF(t) = \frac{1}{2IN^{MG}} \left[r^W(t) + r^S(t) - r^D(t) \right]. \tag{26}$$

Additionally, given the focus of this paper on isolated microgrid daily operations, i.e., without contingencies, one can assume that the continuous-time short-term fluctuations $r(t)$ change linearly between each short time interval $j \in \mathcal{J}$, as follows:

$$r(t) = \underbrace{\left(\frac{r_{h,j+1} - r_{h,j}}{\Delta \tau} \right)}_{\partial r_{h,j}} t \quad \forall t \in [0, \Delta\tau] \tag{27}$$

where $r_{h,j}$ is the short-term power fluctuation at short time interval j within dispatch time interval h, as per (1); $\Delta\tau$ is the time-step length of short time intervals $j \in \mathcal{J}$; and ∂r_{hj} is defined as the short-term power fluctuation ramp. Thus, one can replace (27) in (26) to obtain:

$$RoCoF(t) = \frac{1}{2IN^{MG}} \underbrace{\left[\partial r_{h,j}^W + \partial r_{h,j}^S - \partial r_{h,j}^D \right]}_{\partial r_{h,j}^{MG}} t \tag{28}$$

where $\partial r_{h,j}^{MG}$ is the microgrid's net short-term fluctuation ramp.

Similarly to (4), one can use the microgrid's net short-term fluctuation ramp to define a *regulation-ramp reserve need* $\zeta_h^{\boldsymbol{\partial r}}$, which serves as a basis for deriving a RoCoF constraint, and can be defined as follows:

$$\boldsymbol{\partial r}_h^{MG}(\xi) = \hat{p}_h^W \boldsymbol{\partial \tilde{r}}_h^W(\xi) + \hat{p}_h^S \boldsymbol{\partial \tilde{r}}_h^S(\xi) - \hat{D}_h \boldsymbol{\partial \tilde{r}}_h^D(\xi) \tag{29a}$$

$$\text{std}\left(\boldsymbol{\partial r}_h^{MG}\right)^2 = \left(\hat{D}_h \tilde{\sigma}_h^{\boldsymbol{\partial r},D}\right)^2 + \left(\hat{p}_h^W \tilde{\sigma}_h^{\boldsymbol{\partial r},W}\right)^2 + \left(\hat{p}_h^S \tilde{\sigma}_h^{\boldsymbol{\partial r},S}\right)^2 \tag{29b}$$

$$\zeta_h^{\boldsymbol{\partial r}} = \epsilon_{\boldsymbol{\partial r}} \, \text{std}\left(\boldsymbol{\partial r}_h^{MG}\right) \tag{29c}$$

where $\boldsymbol{\partial \tilde{r}}_h^D$, $\boldsymbol{\partial \tilde{r}}_h^W$, and $\boldsymbol{\partial \tilde{r}}_h^S$ are zero-mean random vectors representing the normalized short-term fluctuation ramps of demand, wind generation, and solar generation, respectively; $\tilde{\sigma}_h^{\boldsymbol{\partial r},D} = \text{std}\left(\boldsymbol{\partial \tilde{r}}_h^D\right)$, $\tilde{\sigma}_h^{\boldsymbol{\partial r},W} = \text{std}\left(\boldsymbol{\partial \tilde{r}}_h^W\right)$, and $\tilde{\sigma}_h^{\boldsymbol{\partial r},S} = \text{std}\left(\boldsymbol{\partial \tilde{r}}_h^S\right)$; and $\epsilon_{\boldsymbol{\partial r}}$ is a parameter for adjusting the desired confidence level.

Based on (29), a constraint for ensuring a proper RoCoF performance can be derived. Such constraint is obtained by replacing $\partial r_{h,j}^{MG}$ in (28) by $\zeta_h^{\boldsymbol{\partial r}}$, and assuming that automatic frequency controllers will not act until $t = T^{FC}$ due to their inherent time delay. This yields the following constraint for ensuring RoCoF limit compliance:

$$\zeta_h^{\boldsymbol{\partial r}} \leq \frac{2\,\overline{RoCoF}}{T^{FC} f_0} \underbrace{\sum_{g \in \mathcal{G}} u_{g,h} IN_g^G}_{IN^{MG}} \quad \forall h \in \mathcal{H} \tag{30}$$

where IN_g^G is the synchronous inertia provided by each available generator g, and $\overline{RoCoF}$ is the absolute RoCoF limit in Hz/s. Note that battery virtual inertia IN^B is not considered in (30), as this type of inertia is affected by converter control time delays and thus is not immediately available for instantaneous RoCoF damping (see Fig. 3).

It is important to highlight that modern frequency-constrained operational models for bulk power systems typically also consider a frequency nadir constraint to limit frequency deviations, as such constraint plays a significant role in the presence of stepwise power disturbances resulting from outages [13]–[17]. However, such type of constraint is not considered here, since: (i) this paper focuses on short-term power fluctuations stemming from renewable generation and

loads, which change in a linear, instead of stepwise, manner; and (ii) unlike bulk power systems, major contingencies such as large generator outages are typically not considered in isolated microgrid dispatch models, as including these would result in impractical large operational costs. The validity of using Quasi-Steady-State (QSS) frequency constraints (21)-(24) and RoCoF constraint (30) for modeling frequency and RoCoF dynamics in isolated microgrid daily operations is discussed in Section IV-E.

D. Renewable Curtailment

Following the approach in [12], the impact of renewable generation in reserve needs is incorporated here through the following equations, which are based on reserve needs (3), (4) and (29):

$$\zeta_h = \epsilon \left[\left(\hat{D}_h \tilde{\sigma}_h^D \right)^2 + \left(\hat{p}_h^W \tilde{\sigma}_h^W \right)^2 + \left(\hat{p}_h^S \tilde{\sigma}_h^S \right)^2 \right]^{1/2} \tag{31a}$$

$$\hat{p}_h^W \leq \overline{P}_h^W, \quad \hat{p}_h^S \leq \overline{P}_h^S \qquad \forall h \in \mathcal{H} \tag{31b}$$

where $\overline{P}_h^W$ and $\overline{P}_h^S$ are, respectively, the maximum available wind and solar average powers during dispatch time interval h; and sub/superscripts $\chi, \boldsymbol{r}, \boldsymbol{\partial r}$ have been omitted in (31a), as the equation is valid for these three cases. Note that unlike [12], (31a) also incorporates the impact of renewable curtailment on regulation-ramp reserve need $\zeta_h^{\boldsymbol{\partial r}}$. Furthermore, observe that similar to [12], (31a) can be convexified by exploiting the fact that the demand D_h, and thus the argument of the square root function, is large enough for practical isolated microgrids. This allows approximating the square root function by a linear interpolation between points $(0, 0)$ and $(\overline{P}^W, \overline{P}^S)$, making (31a) convex, and hence representable by a cutting-planes algorithm [24].

E. Other Constraints

The remainder of the constraints considered for the proposed EMS model are discussed next, closely resembling the ones present in conventional EMS models, such as [1]–[3]. Thus, the power balance is given as follows $\forall h \in \mathcal{H}$:

$$\sum_{b \in \mathcal{B}} \sum_{l \in \mathcal{L}} \left(d_{b,l,h} - c_{b,l,h} \right) + \sum_{g \in \mathcal{G}} \hat{p}_{g,h}^G = \hat{D}_h - \hat{p}_h^W - \hat{p}_h^S - ls_h \tag{32}$$

Furthermore, the logic of commitment variables, and the minimum up and minimum down constraints on thermal generators can be modeled by the following equations $\forall g \in \mathcal{G}, h \in \mathcal{H}$:

$$u_{g,h} - u_{g,h-1} = v_{g,h} - w_{g,h} \tag{33a}$$

$$\sum_{m=h-M_g^{DN}}^{h-1} \left(1 - u_{g,m}\right) \Delta T_m \geq M_g^{DN} \, v_{g,h} \tag{33b}$$

$$\sum_{m=h-M_g^{UP}}^{h-1} u_{g,m} \, \Delta T_m \geq M_g^{UP} \, w_{g,h} \tag{33c}$$

where $v_{g,h}$ and $w_{g,h}$ indicate the start-up and shut-down of generators, respectively; and, M_g^{UP} and M_g^{DN} are the minimum up and minimum down times. Additionally, generator ramp constraints are also considered, which can be defined as follows $\forall g \in \mathcal{G}, h \in \mathcal{H}$:

$$-R_g \, \Delta T_h - \overline{P}_g^G w_{g,h} \leq \hat{p}_{g,h}^G - \hat{p}_{g,h-1}^G \leq R_g \, \Delta T_h + \overline{P}_g^G v_{g,h} \tag{34}$$

where R_g is the generator's ramp limit. Finally, an energy neutrality constraint is included as follows:

$$s_{b,l,H} = S_{b,l}^0 \quad \forall b \in \mathcal{B}, l \in \mathcal{L} \tag{35}$$

where $S_{b,l}^0$ is the initial battery SoC, and H is the last time index of the set of dispatch time intervals $\mathcal{H} = \{1, \ldots, H\}$.

F. Optimization Model

The proposed EMS model can be formulated using the equations presented in the previous sections. The EMS's objective function $\mathcal{F}(\cdot)$ includes a battery degradation component $\Phi \in [0, 1]$, variable generation costs C^G, no-load costs C^{NL}, start-up costs C^{SU}, shut-down costs C^{SD}, and load shedding costs C^{LS}, as follows:

$$\begin{aligned} \mathcal{F}(\boldsymbol{x}, \boldsymbol{y}) = & \sum_{h \in \mathcal{H}} \sum_{b \in \mathcal{B}} \sum_{l \in \mathcal{L}} E_b \cdot RC_b \cdot \Phi_{b,l,h} + \sum_{h \in H} C^{LS} \Delta T_h \, ls_h \\ & + \sum_{h \in \mathcal{H}} \sum_{g \in \mathcal{G}} C_g^G \Delta T_h \left(\hat{p}_{g,h}^G + \Delta e_{g,h} \right) + \\ & \sum_{h \in \mathcal{H}} \sum_{g \in \mathcal{G}} \left(C_g^{NL} \Delta T_h \, u_{g,h} + C_g^{SU} v_{g,h} + C_g^{SD} w_{g,h} \right) \end{aligned}$$

where RC_b is the battery replacement cost; $\boldsymbol{x} = [\boldsymbol{u}, \boldsymbol{v}, \boldsymbol{w}]^T$ are the binary decision variables; and $\boldsymbol{y} = [\hat{\boldsymbol{p}}, \Delta \boldsymbol{p}, \boldsymbol{s}, \boldsymbol{c}, \boldsymbol{d}, \boldsymbol{ls}, \boldsymbol{\zeta}]^T$ are the continuous decisions variables. This results in the following optimization model for the proposed EMS:

$$\begin{aligned} \min_{\boldsymbol{x}, \boldsymbol{y}} \quad & \mathcal{F}(\boldsymbol{x}, \boldsymbol{y}) \\ \text{s.t.} \quad & \boldsymbol{x} \in \{0, 1\}^n, \ \boldsymbol{y} \geq 0 \\ & \text{Reserves and power balance (10), (11), (31), (32)} \\ & \text{Thermal generators (6), (15), (33), (34)} \\ & \text{Batteries and degradation (7)-(9), (16)-(20), (35)} \\ & \text{Frequency dynamics (21)-(24), (30)} \end{aligned}$$

which is a Mixed Integer Linear Programming (MILP) problem that can be solved using efficient off-the-shelf solvers.

G. Architecture and Implementation

The general layout of the proposed EMS is illustrated in Fig. 8, which incorporates the optimization model described in Section III-F (UC-EMS) for determining the dispatch set-points of the microgrid's DER units, as in the case of actual EMS implementations [25]. The proposed EMS follows a Model Predictive Control (MPC) scheme, for which optimal dispatch set-points are regularly re-calculated and broadcasted to the microgrid's local controllers based on frequently updated forecasts and state measurements. Similar to [1]–[3], an MPC update rate of 5min is considered in this work, which allows sufficient time for re-running the forecast engine and retrieving updated state measurements. Thus, every 5 minutes

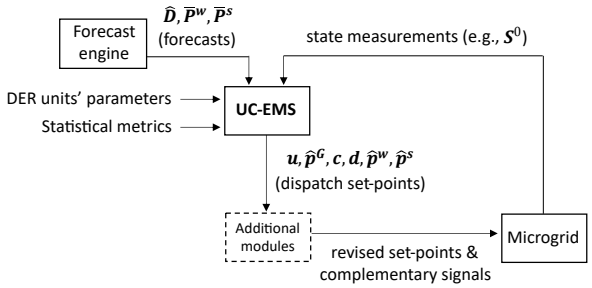


Fig. 8. EMS architecture based on a Model Predictive Control approach.

the UC-EMS optimization model is re-solved and new dispatch set-points are obtained.

It is important to highlight that the architecture described in Fig. 8 allows the incorporation of additional modules for handling other possibly relevant aspects not modeled in the UC-EMS optimization model. For example, an additional Optimal Power Flow module with AC power flow equations can be included to compute reactive power dispatch set-points, as in [1].

IV. Computational Experiments

In this section, multiple simulations are carried out to evaluate the performance of the proposed EMS model. First, the general settings of the simulations and case studies are presented in Sections IV-A and IV-B. Then, the performance of the proposed EMS model is evaluated from four different perspectives, namely regulation security in Section IV-C, operational performance in Section IV-D, frequency modeling accuracy in Section IV-E, and computational performance in Section IV-F.

A. General Settings

The performance of the proposed EMS model is evaluated by simulating its implementation during one full day on a modified CIGRE medium voltage benchmark system based on [12], which has a 6153 kW peak demand and a 50% renewable energy share (25% wind and 25% solar) for the simulated day, and is composed of 3 diesel generators (4700 kW combined capacity), 2 combined heat-and-power units (810 kW combined capacity), and a single 2500kW/2500kWh lithium-ion battery. As per [1]–[3], [12], simulations are performed using an MPC scheme with an update rate of 5min. In each MPC run, a horizon of 24h is considered, which has a variable time resolution with the following time-steps: 6 time-steps of 5min, 6 time-steps of 15min, 6 time-steps of 30min, and 19 time-steps of 1h. Reserve need constraints are enforced only for the next 5 hours in each MPC iteration to reduce computational burden, without significantly impacting optimality.

Residential load, wind power, and solar power data are extracted from [19], which correspond to real measurements obtained from the KLFN microgrid with a time resolution of $\Delta\tau = 1s$. These measurements are split into two different data batches, namely one 6-week-long batch for estimating historical sample standard deviations of short-term fluctuations, and another 1-day-long batch used for simulating the implementation of the proposed EMS. Furthermore, to emulate the presence of uncertain forecast errors in the simulations, a normally distributed random noise is added to the 5min average powers based on the standard deviations reported in [12].

Three different EMS models are considered in the simulations for benchmarking purposes. The first model, referred hereinafter as EMS-1, corresponds to a conventional EMS similar to the ones presented in [1]–[3], for which frequency dynamics and battery degradation are not considered, and uncertain power variations are exclusively handled by a unique total reserve need, without any differentiation for forecast errors or regulation reserve needs. The second model, referred hereinafter as EMS-2, corresponds to the one presented in [12], which incorporates battery degradation and uses forecast error and regulation reserves for power fluctuation management, but does not consider frequency dynamics nor regulation-ramp reserves. The third EMS model, referred hereinafter as EMS-3, corresponds to the proposed EMS model presented in Section III-F, which considers frequency dynamics and battery degradation, and handles uncertain power variations through forecast error, regulation, and regulation-ramp reserves. In both EMS-2 and EMS-3 models, 4 even partitions with $\overline{S}_l = 0.2 \ \forall l \in \mathcal{L}$ are used for representing battery degradation in a piecewise linear manner, as per (5). For the EMS-3 model, constraints (6a)-(6d), (11a) and (21)-(24) are defined only for the first 6 dispatch time intervals with a 5 min time-step, i.e., $\mathcal{H}^r = \{1, \ldots, 6\}$. Note that constraint $\sum_{g \in G} u_{g,h} \geq 1 \ \forall h \in \mathcal{H}$ is included in all three EMS models, which guarantees that at least one diesel generator is dispatched, so that there is always some synchronous inertia available in the system for instantaneous RoCoF damping.

The performance of the three EMS models is evaluated by retrieving the EMS's optimal dispatch set-points for the first dispatch time interval of each MPC iteration, and implementing such set-points in the dynamic model described in Section II-D. Thus, transient simulations are performed iteratively for each dispatch time interval to obtain the evolution of the microgrid's frequency and DER units' instantaneous powers resulting from short-term power fluctuations. These results are then used to compute thermal generation costs, battery degradation costs, load shedding, renewable curtailment, and the amount of time that frequency deviation and RoCoF limits are violated. In accordance with IEEE's DER operating standard [18], all results and analyses related to the RoCoF are performed considering an averaging time window of 0.5s.

To ensure a fair comparison between the three EMS models, reserve needs are calibrated such that: (i) no load shedding resulting from forecast errors is obtained during the simulated day, and (ii) a specified frequency performance in the form of frequency and RoCoF limit compliance is achieved. The first condition is met by considering one standard deviation of the forecast errors when computing the reserve needs of the three EMS models, i.e, $\epsilon_\chi = 1$. The second condition is met by considering an additional total reserve requirement ΔRes in the EMS-1 model, by adjusting $\epsilon_{\boldsymbol{r}}$ in the EMS-2 model, and by

TABLE I
STANDARD DEVIATION OF SHORT-TERM FLUCTUATIONS

Source	5min [%]	15min [%]	30min [%]	1h [%]
Wind	35.43	39.90	42.35	44.58
Solar	16.69	24.54	27.91	33.21
Demand	3.68	6.27	8.93	12.63

TABLE II
STANDARD DEVIATIONS OF SHORT-TERM FLUCTUATION-RAMPS

Source	5min [%]	15min [%]	30min [%]	1h [%]
Wind	8.67	8.16	7.88	7.69
Solar	3.92	3.56	3.23	3.05
Demand	0.71	0.69	0.7	0.68

adjusting both $\epsilon_{\boldsymbol{r}}$ and $\epsilon_{\boldsymbol{\partial r}}$ in the EMS-3 model. The standard deviations of forecast errors $\tilde{\sigma}_h^{\chi}$ are directly extracted from [12], and the standard deviations of short-term flucuations $\tilde{\sigma}_h^{\boldsymbol{r}}$ and fluctuation-ramps $\tilde{\sigma}_h^{\boldsymbol{\partial r}}$ are estimated using the 6-weeks-long batch of the KLFN dataset (see Tables I and II).

A frequency deviation limit of $\overline{\Delta f} = \pm 1.2$Hz, RoCof limit of $\overline{RoCoF} = \pm 0.5$Hz/s, and droop of $\kappa = 5\%$ for all DER units, are considered in the simulations, as per [18]. Frequency and voltage load sensitivities are obtained from the values reported in [26] for residential loads in North America, with $K^{PF} = 0.8$, and $K^{PV} = 1.5$. For RoCoF constraint (30), a frequency controller time delay of $T^{FC} = 0.1$s is considered, which results from the average response time observed for the battery and diesel generators in the transient simulations. For VFC, a voltage limit of $\overline{\Delta V} = 0.01$pu, and proportional gain of $K^{VFC} = 0.2$, are used based on [22]. Diesel engine governor's parameters are extracted from [20], which were slightly tuned to ensure stable system operation.

The battery degradation resulting from the simulations is computed using the procedure and parameters described in [12], for which a detailed representation based on the rainflow cycle counting algorithm is considered. Such degradation is then multiplied by the battery's replacement cost to obtain the resulting battery degradation costs. Load shedding resulting from frequency regulation issues is valuated using a cost of 12 USD/kWh [27], while renewable curtailment is valuated using a cost of 0.07 USD/kWh, which is based on the wind and solar levelized costs of electricity reported in [28]. All simulations are performed on a PC with an Intel Core i7 3.20-GHz processor and 16 GB of RAM under a 64-bit Windows 10 operating system. The EMS optimal dispatch set-points are computed using the Julia programming language [29], JuMP package [30], and Gurobi solver [31]. Transient simulations are performed using MATLAB-Simulink [32].

B. Case Studies and Regulation Security Levels

The three EMS models are evaluated for two different case studies, which aim to illustrate possible practical frequency control configurations in the CIGRE microgrid. The first case study corresponds to the "Base" case, which considers the dynamic model presented in Section II-D, but with the difference that the regulation capability of the VFC has been removed, i.e., $K^{VFC} = 0$ in Fig. 6. The second case study corresponds to the a "Detailed" case, for which the regulation capabilities of the VFC are incorporated, and the original linear percentage-based load shedding controller (see Fig. 4) is replaced by a under-frequency load shedding (UFLS) scheme [33], whose frequency relay settings are illustrated in Fig. 9. In both case studies, three different frequency regulation security levels are considered, which are based on the amount of time where the frequency deviation and RoCoF limits are violated, as follows:

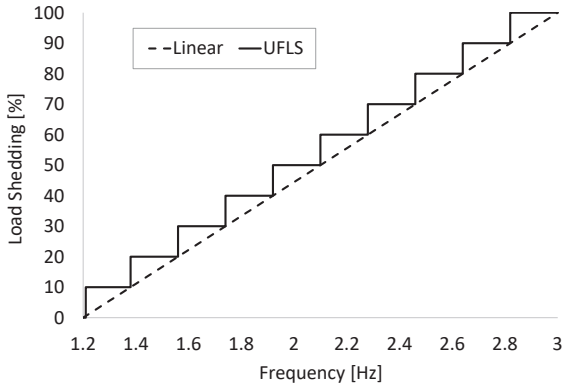


Fig. 9. UFLS frequency relay setting relative to linear percentage-based load shedding controller.

- **Low:** for which frequency limit non-compliance should be around 300s.
- **Medium:** for which frequency limit non-compliance should be around 30s.
- **High:** for which Frequency-or-RoCoF (FoR) limit non-compliance should be around 30s, i.e., the total time that either frequency or RoCoF limits are violated is approximately half a minute.

C. Regulation Security

The capability to reach the Low, Medium, and High regulation security levels is evaluated for the three EMS models in this section. To accomplish this, the reserve requirements of the EMS models are gradually increased until either: (i) the desired frequency/FoR non-compliance is reached, or (ii) an infeasible optimization problem is obtained. The results of this test for the Base and Detailed cases are shown in Tables III and IV, respectively, which include the reserve sizing parameters used in the EMS models, the resulting non-compliance frequency/FoR values, and a flag indicating if the EMS was successful or not in reaching the desired regulation security level. From these results, it can be observed that existing EMS models (EMS-1 and EMS-2) have difficulty reaching high regulation security levels, as these require large reserves that ultimately lead to infeasible optimization problems. In contrast, the proposed EMS model (EMS-3) can attain all regulation levels due to the more accurate modeling of short-term power fluctuations and frequency dynamics, which result in correctly balanced reserve requirements.

TABLE III
SECURITY COMPLIANCE RESULTS FOR BASE CASE

Reg. sec.	EMS Model	Reserve sizing			Non-compl. [s]		Success flag
		ΔRes [MW]	$\epsilon_{\boldsymbol{r}}$	$\epsilon_{\partial r}$	Freq.	FoR	
Low	EMS-1	2.25	-	-	301	378	✓
	EMS-2	-	1.46	-	298	378	✓
	EMS-3	-	1.45	0.0	295	373	✓
Med.	EMS-1	2.59*	-	-	94*	162*	✗
	EMS-2	-	3.45	-	29	81	✓
	EMS-3	-	4.10	0.0	25	78	✓
High	EMS-1	-	-	-	-	-	✗
	EMS-2	-	4.20*	-	2*	46*	✗
	EMS-3	-	4.10	9.0	1	32	✓

*Desired frequency/FoR non-compliance could not be reached. Instead, the minimum achievable non-compliance is indicated.

TABLE IV
SECURITY COMPLIANCE RESULTS FOR DETAILED CASE

Reg. sec.	EMS Model	Reserve sizing			Non-compl. [s]		Success flag
		ΔRes [MW]	$\epsilon_{\boldsymbol{r}}$	$\epsilon_{\partial r}$	Freq.	FoR	
Low	EMS-1	2.00	-	-	302	410	✓
	EMS-2	-	0.54	-	298	405	✓
	EMS-3	-	1.00	0.0	295	399	✓
Med.	EMS-1	2.59*	-	-	62*	144*	✗
	EMS-2	-	3.03	-	30	96	✓
	EMS-3	-	3.33	0.0	30	96	✓
High	EMS-1	-	-	-	-	-	✗
	EMS-2	-	4.20*	-	0*	47*	✗
	EMS-3	-	3.33	9.1	0	32	✓

*Desired frequency/FoR non-compliance could not be reached. Instead, the minimum achievable non-compliance is indicated.

D. Operational Performance

In this section, the operational performance of the three EMS models is evaluated. The results of this test are shown in Tables V and VI for the Base and Detailed cases, respectively, which include: (i) operating costs that consider thermal generation, battery degradation, and load shedding costs; (ii) total costs that include operating and renewable curtailment costs; and (iii) load shedding and renewable curtailment values. Note that the infeasible optimization results identified in Section IV-C are omitted in these tables. From the results, it can be observed that the proposed EMS model (EMS-3) also outperforms existing EMS models (EMS-1 and EMS-2) in terms of operational performance, as the former exhibits reduced operating and total costs (2%-10% lower). Furthermore, note that the proposed EMS model tends to reduce the renewable curtailment in the system (up to 88% lower), which is reflected in the observed reduced costs.

TABLE V
OPERATIONAL RESULTS FOR THE BASE CASE

Reg. sec.	EMS model	Oper. cost [kUSD]	Total cost [kUSD]	Load shed. [kWh]	Ren. curt. [MWh]
Low	EMS-1	9.14	9.19	7.6	0.68
	EMS-2	9.03	9.08	7.1	0.72
	EMS-3	8.60	8.60	9.7	0.08
Med.	EMS-2	10.51	11.02	1.3	7.40
	EMS-3	9.66	10.01	0.5	4.98
High	EMS-3	11.18	11.97	0.1	11.34

TABLE VI
OPERATIONAL RESULTS FOR THE DETAILED CASE

Reg. sec.	EMS model	Oper. cost [kUSD]	Total cost [kUSD]	Load shed. [kWh]	Ren. curt. [MWh]
Low	EMS-1	11.10	11.13	180.3	0.37
	EMS-2	10.18	10.18	130.1	0.05
	EMS-3	9.99	9.99	134.5	0.06
Med.	EMS-2	10.50	10.89	40.1	5.66
	EMS-3	9.67	9.89	39.6	3.22
High	EMS-3	11.24	12.04	6.2	11.47

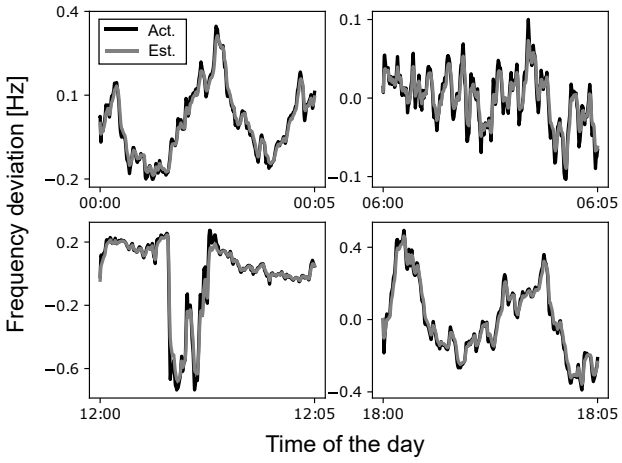


Fig. 10. Comparison of frequency excursions during different times of the day for the Base case using the proposed EMS (EMS-3) under a High regulation security level.

E. Frequency Modeling Accuracy

As previously discussed in Sections I and III-C, one of the major advantages of proposed EMS model lies in the explicit modeling of frequency dynamics. Thus, to further validate the observed results, the accuracy of the QSS frequency equations (21)-(24), and RoCoF equations (28)-(30) used in the proposed EMS model were also tested. For this test, the instantaneous frequency and RoCoF obtained by transient simulations were compared to the ones estimated using (21)-(24) and (28)-(30). Fig. 10 illustrates the actual (Act.) frequency excursions obtained by the transient simulations, and the estimated (Est.) frequency excursions using QSS frequency equations (21)-(24) for a particular simulation case. Note that both actual and estimated curves exhibit a close resemblance, with more significant differences being observed in the presence of abrupt frequency jumps.

The close resemblance between actual and estimated values in Fig. 10 was also observed in the rest of the simulation cases. This is illustrated in Table VII, in which the Mean Absolute Errors (MAE) for all simulations cases are indicated, from where one can conclude that the proposed EMS provides an accurate representation of the actual frequency dynamics of an isolated microgrid during daily operations.

F. Computational Performance

The computational performance of the three EMS models is evaluated here. This is a relevant aspect to assess, as

TABLE VII
FREQUENCY AND ROCOF MEAN ABSOLUTE ERRORS

Reg. sec.	EMS model	Freq. MAE [Hz]		RoCoF MAE [Hz/s]	
		Base	Detailed	Base	Detailed
Low	EMS-1	0.02	0.03	0.04	0.04
	EMS-2	0.01	0.03	0.05	0.04
	EMS-3	0.02	0.03	0.04	0.05
Med.	EMS-2	0.01	0.02	0.02	0.02
	EMS-3	0.01	0.02	0.01	0.02
High	EMS-3	0.01	0.01	0.01	0.01

TABLE VIII
COMPUTATION TIMES PER MPC ITERATION

Reg. sec.	EMS Model	Average time [s]		Maximum time [s]	
		Base	Detailed	Base	Detailed
Low	EMS-1	0.6	0.6	16.9	17.1
	EMS-2	2.0	0.9	21.5	22.2
	EMS-3	1.2	1.0	21.9	24.2
Med.	EMS-2	6.5	5.1	56.7	32.5
	EMS-3	4.5	3.1	27.1	30.7
High	EMS-3	2.9	2.8	18.9	22.7

computation times for the EMS optimization model need to be significantly lower than the 5min MPC update rate for near real-time applications [1]. For this test, the computation times required to solve the optimization problems were recorded for each MPC iteration, yielding a total of 288 measurements for one full day simulation. The resulting average and maximum computation times are presented in Table VIII, where it can be observed that all three EMS models exhibit low computation times in the order of seconds, making them suitable for practical applications. This observed computational efficiency stems from the fact that all three EMS models are linear, and thus result in computationally efficient MILP optimization problems. Therefore, another relevant contribution of the proposed EMS model (EMS-3), is that it incorporates the impact of frequency dynamics on operations while keeping a computational performance on par with the one observed for the simpler EMS-1 and EMS-2 models.

In summary, the proposed EMS model outperforms existing EMS models, achieving reduced operational costs and reaching a wider range of frequency regulation security levels. Moreover, this overall better performance is achieved while keeping computational tractability suitable for near real-time practical applications.

V. CONCLUSION

Short-term power fluctuations stemming from renewable generation can severely degrade the frequency regulation performance of isolated microgrids, as these have low inertia and, more commonly nowadays, significant renewable energy integration. Motivated by this, the present paper developed a practical and computationally efficient EMS that models short-term fluctuations and their impact on frequency regulation and operations. The proposed EMS was evaluated and compared to existing EMSs on a realistic test system, showing that the proposed model allows reducing total operating costs for a given security level (2%-10% lower), and achieving higher frequency regulation security levels in line with modern operating standards for microgrids. Furthermore, thanks to the use of alternative linear equations to describe frequency dynamics, the proposed EMS model can be solved with sufficiently low computation times, making it suitable for near real-time practical applications.

REFERENCES

[1] D. E. Olivares, C. A. Cañizares, and M. Kazerani, "A centralized energy management system for isolated microgrids," *IEEE Trans. Smart Grid*, vol. 5, no. 4, pp. 1864–1875, 2014.

[2] B. V. Solanki, C. A. Cañizares, and K. Bhattacharya, "Practical energy management systems for isolated microgrids," *IEEE Trans. Smart Grid*, vol. 10, no. 5, pp. 4762–4775, 2019.

[3] W. Violante, C. A. Cañizares, M. A. Trovato, and G. Forte, "An energy management system for isolated microgrids with thermal energy resources," *IEEE Trans. Smart Grid*, vol. 11, no. 4, pp. 2880–2891, 2020.

[4] M. F. Zia, E. Elbouchikhi, and M. Benbouzid, "Microgrids energy management systems: A critical review on methods, solutions, and prospects," *Applied Energy*, vol. 222, pp. 1033 – 1055, 2018.

[5] H. Shayeghi, E. Shahryari, M. Moradzadeh, and P. Siano, "A survey on microgrid energy management considering flexible energy sources," *Energies*, vol. 12, no. 11, 2019.

[6] M. Farrokhabadi *et al.*, "Microgrid stability, definitions, analysis, and modeling," IEEE Power and Energy Society, Piscataway, NJ, USA, Tech. Rep. PES-TR66, 2018.

[7] M Anvari *et al.*, "Short term fluctuations of wind and solar power systems," *New Journal of Physics*, vol. 18, no. 6, 2016.

[8] H. Bevrani, A. Ghosh, and G. Ledwich, "Renewable energy sources and frequency regulation: survey and new perspectives," *IET Renewable Power Generation*, vol. 4, no. 5, pp. 438–457, 2010.

[9] Z. Bao *et al.*, "A multi time-scale and multi energy-type coordinated microgrid scheduling solution—part i: Model and methodology," *IEEE Trans. Power Systems*, vol. 30, no. 5, pp. 2257–2266, 2015.

[10] C. Ju, P. Wang, L. Goel, and Y. Xu, "A two-layer energy management system for microgrids with hybrid energy storage considering degradation costs," *IEEE Trans. Smart Grid*, vol. 9, no. 6, pp. 6047–6057, 2018.

[11] C. Zhang, Y. Xu, Z. Y. Dong, and J. Ma, "Robust operation of microgrids via two-stage coordinated energy storage and direct load control," *IEEE Trans. Power Syst.*, vol. 32, no. 4, pp. 2858–2868, 2017.

[12] S. Cordova, C. Canizares, A. Lorca, and D. E. Olivares, "An energy management system with short-term fluctuation reserves and battery degradation for isolated microgrids," *IEEE Transactions on Smart Grid*, pp. 1–1, 2021.

[13] L. Badesa, F. Teng, and G. Strbac, "Simultaneous scheduling of multiple frequency services in stochastic unit commitment," *IEEE Trans. Power Systems*, vol. 34, no. 5, pp. 3858–3868, 2019.

[14] M. Paturet *et al.*, "Stochastic unit commitment in low-inertia grids," *IEEE Trans. Power Systems*, vol. 35, no. 5, pp. 3448–3458, 2020.

[15] Z. Chu, U. Markovic, G. Hug, and F. Teng, "Towards optimal system scheduling with synthetic inertia provision from wind turbines," *IEEE Trans. Power Systems*, vol. 35, no. 5, pp. 4056–4066, 2020.

[16] S. Saberi Oskouee, S. Kamali, and T. Amraee, "Primary frequency support in unit commitment using a multi-area frequency model with flywheel energy storage," *IEEE Trans. Power Systems*, pp. 1–1, 2021.

[17] L. Badesa, F. Teng, and G. Strbac, "Conditions for regional frequency stability in power system scheduling—part II: Application to unit commitment," *IEEE Trans. Power Systems*, pp. 1–1, 2021.

[18] "IEEE standard for interconnection and interoperability of distributed energy resources with associated electric power systems interfaces," *IEEE Std 1547-2018 (Revision of IEEE Std 1547-2003)*, 2018.

[19] M. Arriaga and C. Cañizares, "Overview and Analysis of Data for Microgrid at Kasabonika Lake First Nation (KLFN)," Hatch Project, University of Waterloo, Tech. Rep., 2015.

[20] K. Yeager and J. Willis, "Modeling of emergency diesel generators in an 800 megawatt nuclear power plant," *IEEE Transactions on Energy Conversion*, vol. 8, no. 3, pp. 433–441, 1993.

[21] X. Xu, M. Bishop, D. G. Oikarinen, and C. Hao, "Application and modeling of battery energy storage in power systems," *CSEE Journal of Power and Energy Systems*, vol. 2, no. 3, pp. 82–90, 2016.

[22] M. Farrokhabadi, C. A. Cañizares, and K. Bhattacharya, "Frequency control in isolated/islanded microgrids through voltage regulation," *IEEE Transactions on Smart Grid*, vol. 8, no. 3, pp. 1185–1194, 2017.

[23] J.-F. Toubeau *et al.*, "Data-driven scheduling of energy storage in day-ahead energy and reserve markets with probabilistic guarantees on real-time delivery," *IEEE Transactions on Power Systems*, pp. 1–1, 2020.
[24] S. Boyd and L. Vandenberghe, "Localization and cutting-plane methods," Stanford EE 364b course, Lecture notes, 2007.
[25] Hatch Ltd, "Hybrid Power," Brochure, 2017. [Online]. Available: https://www.hatch.com/-/media/Hatch-Corporate/Brochures/HybridPower_Brochure.pdf
[26] L. M. Korunovic *et al.*, "Recommended parameter values and ranges of most frequently used static load models," *IEEE Transactions on Power Systems*, vol. 33, no. 6, pp. 5923–5934, 2018.
[27] A. J. Praktiknjo, A. Hähnel, and G. Erdmann, "Assessing energy supply security: Outage costs in private households," *Energy Policy*, vol. 39, no. 12, pp. 7825 – 7833, 2011.
[28] "Renewable power generation costs in 2019," International Renewable Energy Agency, Tech. Rep., 2019.
[29] J. Bezanson, A. Edelman, S. Karpinski, and V. B. Shah, "Julia: A fresh approach to numerical computing," *SIAM review*, vol. 59, no. 1, pp. 65–98, 2017.
[30] I. Dunning, J. Huchette, and M. Lubin, "JuMP: A modeling language for mathematical optimization," *SIAM Review*, vol. 59, no. 2, pp. 295–320, 2017.
[31] Gurobi Optimization, LLC, "Gurobi Optimizer Reference Manual," 2021. [Online]. Available: https://www.gurobi.com
[32] MATLAB, *version 9.10.0 (R2021a)*. Natick, Massachusetts: The MathWorks Inc., 2021. [Online]. Available: https://www.mathworks.com
[33] N. N. A. Bakar *et al.*, "Microgrid and load shedding scheme during islanded mode: A review," *Renewable and Sustainable Energy Reviews*, vol. 71, pp. 161–169, 2017.



Samuel Córdova (S'18) received the M.Sc. degree in electrical engineering from the Pontificia Universidad Católica de Chile (Santiago, Chile) and is currently working towards a Ph.D. degree in electrical engineering at both the University of Waterloo (Waterloo, ON, Canada) and Pontificia Universidad Católica de Chile under a cotutelle agreement. He has worked as a R&D Engineer at the Systep Ingeniería and Vinken consulting firms in Chile and performed various studies for the Chilean system operator. His main research interest include the operation and control of modern power systems with significant renewable integration in the context of smart grids.



Claudio Cañizares (S'85-M'91-SM'00-F'07) is a University Professor, the Hydro One Endowed Chair, and the Executive Director of the Waterloo Institute for Sustainable Energy (WISE) at the ECE Department of the University of Waterloo, where he has been since 1993. His highly cited research focuses on modeling, simulation, computation, stability, control, and optimization of power and energy systems. He is the IEEE Trans. Smart Gird EIC; Division VII Director-Elect to the IEEE Board; a Fellow of the IEEE, the Royal Society of Canada, and the Canadian Academy of Engineering; and has received the 2017 IEEE PES Outstanding Power Engineering Educator Award, the 2016 IEEE Canada Electric Power Medal, and multiple awards and recognitions from PES Technical Committees.



Álvaro Lorca (M'17) is an Assistant Professor in the Department of Electrical Engineering and the Department of Industrial and Systems Engineering at Pontificia Universidad Católica de Chile. He is also co-director of Vinken, a business unit at Dictuc dedicated to specialized consulting, advanced research, and technological developments for the energy industry. He received a Ph.D. in Operations Research from Georgia Institute of Technology, and an M.Sc. in Engineering and an Industrial Engineering degree with a diploma in Mathematical Engineering from Pontificia Universidad Católica de Chile. His research and professional activities are centered in the application of mathematical methods and data science in energy planning, power system operations, renewable energy integration, smart grids, and resilience, among other topics. He has published in various specialized scientific journals, including Operations Research, European Journal of Operational Research, Production and Operations Management, IEEE Transactions on Power Systems, Energy, Energy Economics, Applied Energy, and Energy Policy, among others. He has worked with ISO New England, World Bank, Environmental Defense Fund, Coordinador Eléctrico Nacional, Comisión Nacional de Energía, Chilean Ministry of Energy, Transelec, and Fraunhofer Chile Research, among others. His research has been recognized with various awards, including the Best Paper in Energy Award from the INFORMS Section on Energy, Natural Resources, and the Environment, and the Best Paper Award from the IEEE Power and Energy Society.



Daniel E. Olivares (S'11-M'14) was born in Santiago, Chile. He received the B.Sc. and Engineering degrees in electrical engineering from the University of Chile, Santiago, in 2006 and 2008, respectively, and the Ph.D. degree in electrical and computer engineering from the University of Waterloo, Waterloo, ON, Canada, in 2014. He is currently an Associate Professor in the Faculty of Engineering and Sciences at Adolfo Ibañez University, Chile. His research interests include modeling, simulation, and control, and optimization of power systems in the context of smart grids.